



Denoising Diffusion Post-Processing for Low-Light Image Enhancement

Savvas Panagiotou , and Anna S. Bosman , *Member, IEEE*

Abstract—Low-light image enhancement (LLIE) techniques attempt to increase the visibility of images captured in low-light scenarios. However, as a result of enhancement, a variety of image degradations such as noise and color bias are revealed. Furthermore, each particular LLIE approach may introduce a different form of flaw within its enhanced results. To combat these image degradations, post-processing denoisers have widely been used, which often yield oversmoothed results lacking detail. We propose using a diffusion model as a post-processing approach, and we introduce Low-light Post-processing Diffusion Model (LPDM) in order to model the conditional distribution between under-exposed and normally-exposed images. We apply LPDM in a manner which avoids the computationally expensive generative reverse process of typical diffusion models, and post-process images in one pass through LPDM. Extensive experiments demonstrate that our approach outperforms competing post-processing denoisers by increasing the perceptual quality of enhanced low-light images on a variety of challenging low-light datasets. Source code is available at <https://github.com/savvaki/LPDM>.

Index Terms—Diffusion model, denoising, low-light image enhancement, post-processing

I. INTRODUCTION

THE task of low-light image enhancement (LLIE) aims to improve the visibility of images which are captured under low-light conditions. Under-exposed images are often degraded in a variety of ways in addition to their lack of visibility. Notably, low-light regions of an image typically contain degraded color information, a lack of detail as well as intensive noise. LLIE techniques aim to brighten low-light regions of an image while maintaining color accuracy and minimizing noise. The demand for brightening and enhancing low-light images often arises due to many downstream algorithms only being performant on images with high-visibility [1]. Some of these downstream tasks include object detection [2], facial recognition [3], surveillance [4] and semantic segmentation [5].

Simply adjusting the contrast of low-light images using a technique such as histogram equalization [6] is often insufficient due to the amplification of noise [1], [7]. Learning-based methods have emerged which significantly outperform traditional methods. However, even the state-of-the-art deep learning (DL) techniques still introduce a variety of artifacts in different scenarios [8].

Existing denoising techniques can be applied to denoise low-light images either before or after contrast enhancement [9], [10]. These denoising techniques range from low-pass

filters and algorithms such as block matching and 3D filtering (BM3D) [11], to state-of-the-art DL denoisers [9], [12]. Despite denoisers significantly reducing noise, they often introduce blurriness into the denoised output. As a result, removing the amplified noise in a brightened low-light image often comes at the cost of removing detail, especially in high-frequency regions of the image.

We propose a post-processing conditional diffusion model (DM) [13] with the capability of removing unwanted noise and other distortions in brightened low-light images. We name our conditional model Low-light Post-processing Diffusion Model (LPDM). The effect of post-processing using LPDM is displayed in Fig. 1. Our technique is able to avoid the computationally expensive generative diffusion reverse process and denoise a given image in one pass through the model. Furthermore, LPDM is often able to improve the sharpness and color accuracy of the enhanced image. In summary, our contributions are as follows:

- 1) We introduce a method of applying DMs as a post-processing technique in the LLIE pipeline. Our framework is able to circumvent the computationally expensive iterative reverse process of DMs and denoise images in one pass through the model.
- 2) We demonstrate that our DM improves existing state-of-the-art LLIE techniques on popular low-light datasets including challenging unpaired test sets.
- 3) In addition to simple denoising, we demonstrate that our method is able to cope with a variety of different artifacts and color distortions, yielding superior results to existing denoisers for LLIE.

The remainder of this paper is structured as follows: Section II provides background information on LLIE; Section III provides background information on DMs; Section IV outlines preliminary mathematical notation and describes the proposed framework in detail; Section V contains the experimental setup and results for this work, including an ablation study; finally, conclusions are drawn in Section VI.

II. LOW-LIGHT IMAGE ENHANCEMENT

LLIE techniques have existed for many decades and can be divided into non-learning-based methods and learning-based methods. Popular examples of traditional techniques which do not require learning from data include variants of histogram equalization (HE) [6], [20] and gamma correction (GC) [21]. HE adjusts the global contrast of an image via a single transformation function. However, low-light images often require contrast enhancements that vary dynamically

S. Panagiotou and A.S. Bosman are with the Department of Computer Science, University of Pretoria, Pretoria, Gauteng, South Africa.
E-mail: savva.panagiotou@gmail.com, anna.bosman@up.ac.za

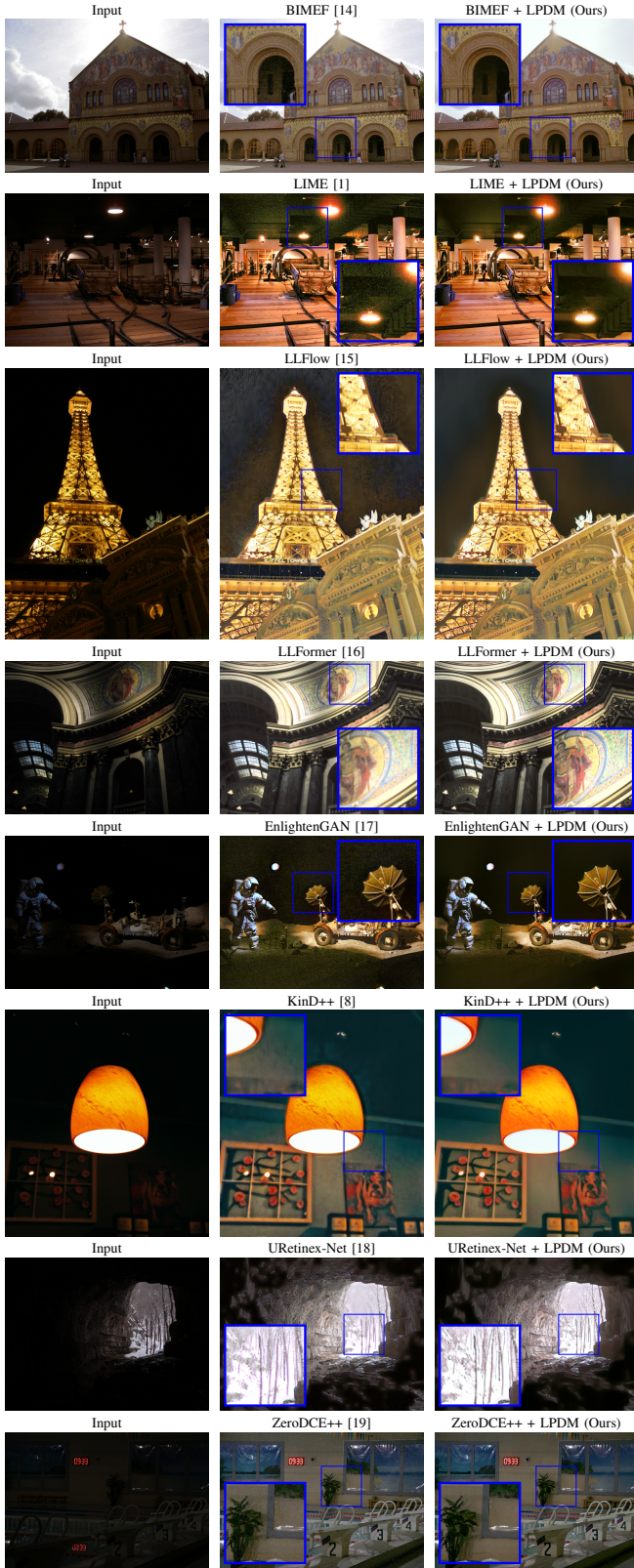


Fig. 1. Qualitative results of our proposed approach on a variety of evaluation datasets for a variety of LLIE methods. **Left:** the input test image. **Middle:** the output of the listed LLIE method for the input image. **Right:** the result of applying our proposed post-processing LPDM to the image from the middle column. The LPDM parameters used are $\phi = 300$ and $s = 30$.

depending on local regions of the image. Thus, techniques such as GC adjust an image via a non-linear per-pixel transform to brighten dark regions while leaving bright regions relatively unaffected. Despite achieving reasonable results, the abovementioned traditional methods often require post-processing techniques in order to deal with amplified noise after enhancement, and struggle to perform well across diverse scenes.

Another paradigm of LLIE makes use of Retinex theory, where the assumption is that a color image can be separated into reflectance and illumination [22]. Non-learning Retinex-based methods such as Low-light Image Enhancement via Illumination Map Estimation (LIME) [1] provide an effective image enhancement approach; however, post-processing denoising is typically still necessary using algorithms such as BM3D [11] which often blurs high-frequency details. Alternative Retinex-based methods reformulate the traditional Retinex model to incorporate an added noise term in order to cater for noise [23].

DL methods have recently achieved state-of-the-art LLIE performance. Some complexities of catering for a large variety of realistic low-light scenes are abstracted away by a data-driven approach. Most DL architectures are based on Convolutional Neural Networks (CNNs) and more recently, CNNs have been hybridized with transformer networks [24]. DL methods either opt for incorporating denoising into a single model, or apply denoising as a post-processing step. S-LLNet [4] makes use of a learned denoiser which operates sequentially after contrast enhancement. Retinex-net [25] incorporates Retinex theory into a DL model with an optional illumination-varying BM3D denoiser used as post-processing. Raw sensor data are enhanced and denoised via CNN in [7]. A variety of loss functions have also been proposed (in addition to the typical l_1 and l_2 losses) which further penalize networks based on color, smoothness, brightness and perceptual interpretation [4], [5], [8], [26]–[32]. Unsupervised Generative Adversarial Networks (GANs) have also been proposed for LLIE [17]. Recently, transformer architectures have gained popularity for LLIE which exploit spatial and channel-wise attention mechanisms [16], [33].

Another relevant state-of-the-art approach with respect to this work is the DL model LLFlow [15]. The LLFlow framework learns the conditional distribution between low-light and normally-exposed images via the generative paradigm of normalizing flow [34]. The LLFlow architecture consists of an encoder as well as an invertible network, trained by minimizing negative log likelihood. The encoder of LLFlow produces an illumination-invariant color map as the prior distribution, upon which the invertible network learns to produce a normally-exposed image.

LPDM proposed in this study also models the conditional distribution between low-light and normally-exposed images; however, we use the diffusion paradigm to achieve this. Furthermore, we repurpose the function of a DM to be used as a noise detector. Therefore, LPDM provides a subtractable estimation of the noise in an image which can further enhance the image. In contrast to LLFlow, LPDM is used as a post-processing step which can be applied regardless of the

enhancing step that precedes LPDM.

III. DIFFUSION MODELS

A DM is a form of generative model which has recently been shown to generate high-quality samples, outperforming GANs [13], [35]–[37]. DMs iteratively remove small perturbations of noise, typically starting with a sample from an isotropic Gaussian distribution, until they generate a clean data sample. In this way, the unconditional diffusion process connects a complex data distribution $q(\mathbf{x}_0)$ to a simpler, analytically tractable, distribution via a Markov chain consisting of a finite number of timesteps T [35]. The subscript of a sample indicates a timestep in the Markov chain, with 0 being a clean sample and T being a sample with the maximum amount of noise added. DMs have been successfully used to model both unconditional and conditional distributions [36], [38]. In spite of the impressive results of DMs, the speed of generating samples has always been a drawback due to their iterative reverse process. Attempts have been made to increase sample speed by making the sampling process non-Markovian, as well as moving DMs to the latent space [39], [40].

We avoid using DMs for sampling normally-exposed images owing to their expensive generative reverse process. Instead, we exploit the ability of DMs to capture complex conditional data distributions. In particular, we use DMs to capture the relationship between under-exposed and normally-exposed images. Other work has shown that DMs may be used as backbone feature extractors which predict features based on noisy inputs [41], [42]. Furthermore, the task of denoising itself has been shown to assist with seemingly unrelated tasks such as semantic segmentation [43]. The applications of using DMs in the field of LLIE are relatively unexplored, especially considering that LLIE can be posed as a denoising problem.

IV. METHODOLOGY

In this work, we propose a technique where a conditional DM is used to remove noise from images which have undergone LLIE. The remainder of this section is structured as follows: in Section IV-A, the background information about DMs is outlined; the architecture used for LPDM is described in Section IV-B; finally, in Section IV-C, we provide detail of our proposed framework.

A. Preliminaries

DMs make use of a forward process which adds noise to a sample and a reverse process which removes noise. Our goal is to model the conditional data distribution $\mathbf{x}_0 \sim q(\mathbf{x}_0|\mathbf{c})$, where \mathbf{c} is an under-exposed image and \mathbf{x}_0 is a normally-exposed image. The forward diffusion process is defined as follows [13]:

$$\begin{aligned} q(\mathbf{x}_{1:T}|\mathbf{x}_0) &:= \prod_{t=1}^T q(\mathbf{x}_t|\mathbf{x}_{t-1}), \\ q(\mathbf{x}_t|\mathbf{x}_{t-1}) &:= \mathcal{N}(\mathbf{x}_t; \sqrt{1-\beta_t}\mathbf{x}_{t-1}, \beta_t\mathbf{I}), \end{aligned} \quad (1)$$

where $\beta_t \in (0, 1)$ defines a variance to be used at timestep t . As seen by the Markov chain in Eq. (1), obtaining a more noisy

sample \mathbf{x}_t is dependent on the previous less-noisy sample \mathbf{x}_{t-1} . Defining extra notation $\alpha_t := 1 - \beta_t$ and $\bar{\alpha}_t := \prod_{s=1}^t \alpha_s$ allows for Eq. (1) to be reformulated to be conditioned on the original clean data sample \mathbf{x}_0 [13]:

$$q(\mathbf{x}_t|\mathbf{x}_0) := \mathcal{N}(\mathbf{x}_t; \sqrt{\bar{\alpha}_t}\mathbf{x}_0, (1 - \bar{\alpha}_t)\mathbf{I}). \quad (2)$$

The efficient sampling of an arbitrary \mathbf{x}_t at any timestep in the Markov chain is possible given \mathbf{x}_0 :

$$\mathbf{x}_t = \sqrt{\bar{\alpha}_t}\mathbf{x}_0 + \sqrt{1 - \bar{\alpha}_t}\boldsymbol{\epsilon}, \quad (3)$$

where $\boldsymbol{\epsilon} \sim \mathcal{N}(0, 1)$ is a random source. The variance schedule is designed such that $\mathbf{x}_T \approx \mathcal{N}(0, 1)$. Conditional DMs model the reverse process $p_\theta(\mathbf{x}_{t-1}|\mathbf{x}_t, \mathbf{c})$ where θ indicates that the DM is modelled by a neural network parameterized by θ . The conditional DM attempts to maximize the likelihood $p_\theta(\mathbf{x}_0|\mathbf{c})$. The reverse diffusion process is defined by parameterized Gaussian transitions [13]:

$$\begin{aligned} p_\theta(\mathbf{x}_{0:T}|\mathbf{c}) &:= p(\mathbf{x}_T) \prod_{t=1}^T p_\theta(\mathbf{x}_{t-1}|\mathbf{x}_t, \mathbf{c}), \\ p_\theta(\mathbf{x}_{t-1}|\mathbf{x}_t, \mathbf{c}) &:= \mathcal{N}(\mathbf{x}_{t-1}; \boldsymbol{\mu}_\theta(\mathbf{x}_t, t, \mathbf{c}), \boldsymbol{\Sigma}_\theta(\mathbf{x}_t, t, \mathbf{c})). \end{aligned} \quad (4)$$

In order to avoid learning the variance, let $\boldsymbol{\Sigma}_\theta(\mathbf{x}_t, t, \mathbf{c}) = \sigma_t^2\mathbf{I}$, where $\sigma_t^2 = \frac{1-\bar{\alpha}_{t-1}}{1-\bar{\alpha}_t}\beta_t$ is a time-dependent constant [13]. Therefore, the only learnable component is $\boldsymbol{\mu}_\theta$. Instead of directly predicting $\boldsymbol{\mu}_\theta$, the DM is parameterized in terms of a denoising autoencoder $\boldsymbol{\epsilon}_\theta(\mathbf{x}_t, t, \mathbf{c})$ where $t = 1, \dots, T$. The number of timesteps T is set to a large number (such as $T = 1000$) in order for the reverse process to better approximate a Gaussian distribution [39]. The corresponding simplified objective is as follows [13]:

$$L_{DM} = \mathbb{E}_{\mathbf{x}_0, \mathbf{c}, \boldsymbol{\epsilon}, t} [\|\boldsymbol{\epsilon} - \boldsymbol{\epsilon}_\theta(\sqrt{\bar{\alpha}_t}\mathbf{x}_0 + \sqrt{1 - \bar{\alpha}_t}\boldsymbol{\epsilon}, t, \mathbf{c})\|^2], \quad (5)$$

where t is uniformly sampled from $\{1, \dots, T\}$ and $\boldsymbol{\epsilon} \sim \mathcal{N}(0, 1)$. In simplified terms, L_{DM} guides the DM to predict the underlying $\boldsymbol{\epsilon}$ that was involved in sampling \mathbf{x}_t . Given \mathbf{x}_t and a prediction for $\boldsymbol{\epsilon}$ using $\boldsymbol{\epsilon}_\theta$, we can calculate an estimate of \mathbf{x}_0 [13]:

$$\mathbf{x}_0 \approx \hat{\mathbf{x}}_0 = \frac{1}{\sqrt{\bar{\alpha}_t}}\mathbf{x}_t - \left(\sqrt{\frac{1}{\bar{\alpha}_t}} - 1\right)\boldsymbol{\epsilon}_\theta(\mathbf{x}_t, t, \mathbf{c}). \quad (6)$$

Further information about the DM sampling process is omitted since it is not used in this work.

B. Diffusion Model Architecture

The DM architecture $\boldsymbol{\epsilon}_\theta$ used for modelling the diffusion process is typically a form of modified U-Net [13], [44]. By definition, a U-Net consists of an encoder and a decoder. The encoder contains a set of residual blocks [45] followed by downsampling operations which are repeated multiple times until the desired latent resolution is achieved. The decoder consists of residual blocks followed by upsampling operations in order to return the latent encoding to the original input

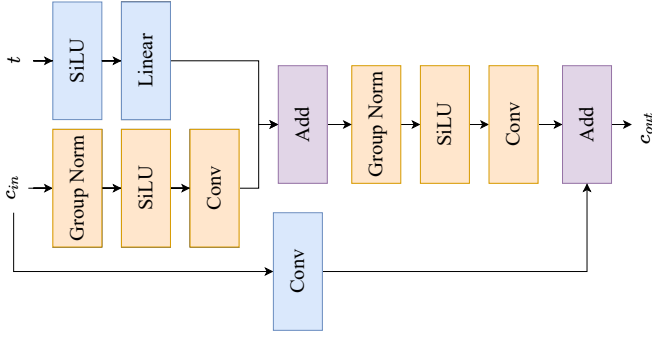


Fig. 2. Residual block used throughout the DM architecture consisting of a combination of group normalization layers, SiLU activations, convolution layers and addition operations. Both c_{in} and t are inputs to the residual block and represent the channel and timestep-embedded input respectively. Note that t is already in embedded form when it enters the residual block. The output of the residual block is represented by c_{out} .

resolution. Each downsampling stage halves the input resolution and each upsampling stage doubles the input resolution. Before each set of residual blocks in the decoder, output from the encoder with the corresponding resolution is concatenated such that spatial context is not lost as a result of the downsampling operations. Between the encoder and decoder is a middle block which contains a specified number of residual blocks in order to process the latent encoding.

The DM operates across all timesteps in the Markov chain using the same parameters. This is made possible by modifying the original U-Net to condition on timestep information represented by sinusoidal positional embeddings as seen in transformer networks [13], [24]. Other notable modifications from the original U-Net are the use of attention mechanisms at different spatial resolutions as well as the use of group normalization [46] within the residual blocks. As seen in Fig. 2, the residual blocks of the DM are composed of a combination of group normalization layers, SiLU activations [47], convolutional layers and addition operators. A variety of attention mechanisms may be applied at different spatial resolutions, such as global attention [48], cross-attention [49] or scaled dot-product attention [24].

C. Proposed Framework

In order to address possible degradations which occur after LLIE, we propose LPDM represented by ϵ_θ . The LPDM model is given $(x_t \oplus c, t)$ as input and tasked with predicting ϵ , where $x_t \sim q(x_t|x_0)$ is a normally-exposed image with noise $\epsilon \sim \mathcal{N}(0,1)$ added at a timestep t , c is the corresponding under-exposed image and \oplus is the concatenation operator.

We follow the common DM training process where the LPDM is exposed to batches of $(x_t \oplus c, t)$ with randomly sampled t for each sample in a batch. A visualization of the training process is depicted in the left half of Fig. 4. After the LPDM has been trained, the LPDM is applied in a novel manner. Specifically, the LPDM acts as a noise detector given an enhanced low-light image. Let η be any low-light image enhancer and let \hat{x}_0^η be an enhanced image such that $\hat{x}_0^\eta = \eta(c)$. The LPDM is used to obtain an estimate of the noise present in \hat{x}_0^η :

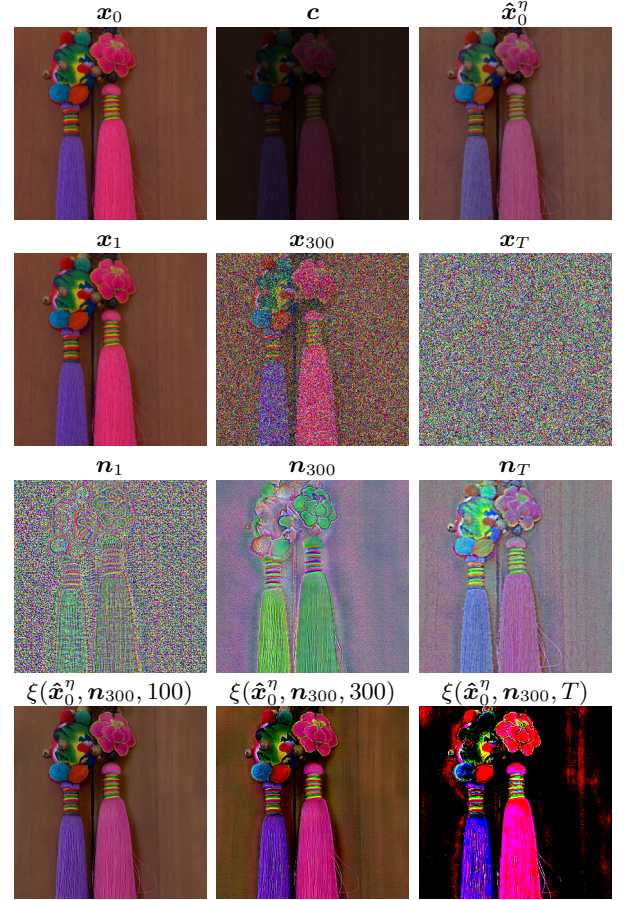


Fig. 3. Visualization of different components within the diffusion process and the LPDM pipeline. The first row displays a normally-exposed image, under-exposed image and image which has undergone LLIE. The second row demonstrates how noise is added to x_0 using a linear variance schedule during the training process, with $T = 1000$. The third row demonstrates the effect of different values of ϕ in Eq. (7). The fourth row demonstrates the effect of applying Eq. (8) with different values of s in order to enhance \hat{x}_0^η .

$$n_\phi = \epsilon_\theta(\hat{x}_0^\eta, \phi, c), \quad (7)$$

where $\phi < T$ is a timestep at which we wish to detect noise in \hat{x}_0^η . An important property of Eq. (7) is that noise is not added to \hat{x}_0^η ; rather, the model is tasked with finding the noise present in \hat{x}_0^η as a result of enhancement, based on the conditioning c and timestep ϕ . Additionally, the value of ϕ is selected at a level such that the underlying structure of the image would be preserved if noise were hypothetically to be added. Thus, a suitable value for ϕ is related to the selected variance schedule. Fig. 3 provides visual examples of applying our proposed approach for an example set of x_0 , c and \hat{x}_0^η . Row 2 of Fig. 3 demonstrates the effect of selecting different values of t in Eq. (2) in order to sample a noisy image during the training process. The noise schedule closer to 0 corresponds to less added noise in the image. Therefore, it is reasonable to expect noise in \hat{x}_0^η at lower levels of ϕ since we do not expect \hat{x}_0^η to be pure noise.

Row 3 of Fig. 3 demonstrates the effect of different values of ϕ . For values of ϕ that are too low, the model overestimates the noise present in \hat{x}_0^η . For large values of ϕ , the model becomes

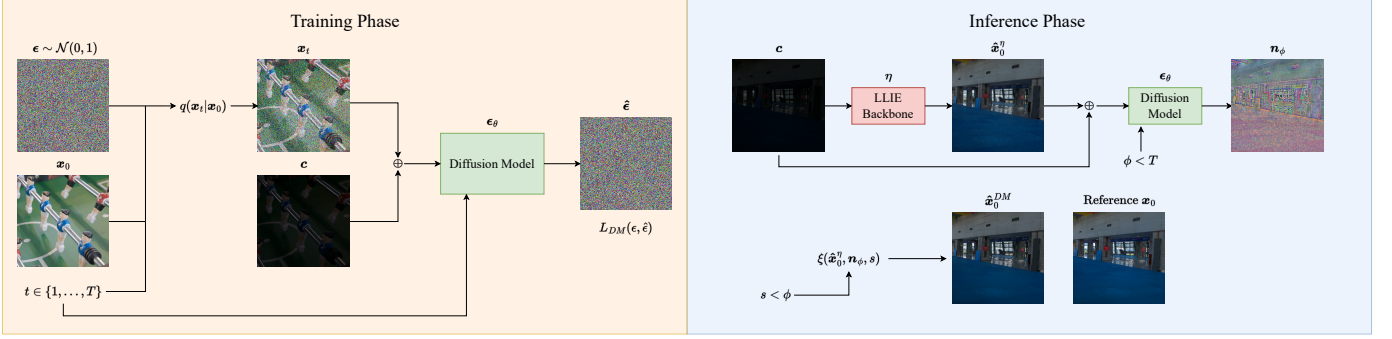


Fig. 4. Diagram presenting the training phase and inference phase of the LPDM, displayed on the left and right half of the diagram respectively.

similar to an autoencoder and attempts to predict the input. The reason for the behavior of different levels of ϕ can be explained by how the LPDM is trained. For values of ϕ close to T , the LPDM expects the input to be purely noise, and thus a suitable prediction for ϵ would simply be to predict the input. For low values of ϕ , the model expects subtle noise in the input image and thus may overdetect noise. We find a good balance to be values of ϕ where the background structure of the image is not completely destroyed such as $\phi = 300$ which corresponds to x_{300} in row 2 of Fig. 3.

Once we obtain the estimation of the noise n_ϕ , we subtract the noise from \hat{x}_0^η using a modification of Eq. (6):

$$\hat{x}_0^{DM} = \xi(\hat{x}_0^\eta, n_\phi, s) := \frac{1}{\sqrt{\alpha_s}} \hat{x}_0^\eta - \left(\sqrt{\frac{1}{\alpha_s}} - 1 \right) n_\phi, \quad (8)$$

where s is a timestep which selects the coefficients according to the variance schedule, and thus balances the degree to which noise is subtracted from \hat{x}_0^η . The final result after LPDM post-processing is represented by \hat{x}_0^{DM} . Notably, we find that s should be significantly less than ϕ in order to subtract the correct amount of noise. As $s \rightarrow \phi$, more of the noise n_ϕ is subtracted from \hat{x}_0^η , leading to overcorrections and perhaps further degrading the result. As seen in row 4 of Fig. 3, the value of s impacts how much correction should be applied. Our technique is able to reduce noise, correct color and improve sharpness as seen when comparing \hat{x}_0^η to $\xi(\hat{x}_0^\eta, n_{300}, 100)$ in Fig. 3.

Denoising techniques may be classified as being either blind or non-blind. Blind denoisers do not require the user to specify the level of noise in the input image, whereas non-blind denoisers require the user to specify the noise level. The popular BM3D algorithm is a non-blind approach. Similarly, our approach requires a selection of s to determine to what extent noise should be subtracted, however we find low values of s to be applicable to a wide variety of scenarios.

In summary, our approach requires the specification of a parameter s during application, where ϕ may be fixed empirically. We find $\phi = 300$ to be a reasonable choice, and we use this value for all experiments. As $s \rightarrow 0$, the amount of correction lessens. The right half of Fig. 4 summarizes the inference process described above.

V. EXPERIMENTS

The following subsections outline the experimental setup: Section V-A describes the datasets used in this study; Section V-B defines the configuration of LPDM and the training parameters used for all experiments; Section V-C provides detail on the LLIE models selected for comparison with LPDM; in order to achieve a fair comparison, we compare our approach to alternative denoising methods described in Section V-D; the interpretation of all the results is presented in Section V-E; finally, an ablation study is conducted in Section V-F.

A. Evaluation Datasets

Paired low-light datasets are challenging to collect due to the requirement of having the scene remain unchanged while camera ISO is adjusted [25]. Accordingly, many methods resort to augmenting datasets with synthetic data. Synthetic datasets are typically generated by adjusting the gamma of normally-exposed images and adding simulated noise. We avoid training the LPDM on synthetic datasets in order to ensure that we correctly model the conditional distribution between under-exposed and normally-exposed images. We train on the original paired LOL dataset [25], which contains 485 training images and 15 test images. Alternative versions of LOL exist, however these only add synthetic data such as the extended version of LOL [50] and VE-LOL [3]. We evaluate our model on the widely-adopted real unpaired test sets LIME¹ (10 images) [1], DICM (64 images) [51], MEF (17 images) [52], NPE (7 images) [53]. We specify the number of images explicitly as previous works use varying subsets of the test sets. The full-reference metrics we adopt are structural similarity index measure (SSIM), peak signal-to-noise ratio (PSNR), mean absolute error (MAE) and learned perceptual image patch similarity (LPIPS) [54]. For the unpaired test data we adopt the following no-reference metrics: natural image quality evaluator (NIQE) [55], blind/referenceless image spatial quality evaluator (BRISQUE) [56] and the smartphone photography attribute and quality (SPAQ) database [57]. All metrics are calculated in the RGB color space unless otherwise stated.

¹LIME [1] is both a LLIE technique and an unpaired test dataset, both of which are proposed in the same paper.

B. Implementation Details

A linear variance schedule is used in the range [0.00085, 0.012] for the diffusion process. The value of T is fixed to 1000 for all experiments. The LPDM is trained on the LOL training set for 6000 training steps using the AdamW optimizer [58] with a learning rate of 1×10^{-6} and with the AdamW parameters $\beta_1 = 0.9$, $\beta_2 = 0.999$ and $\lambda = 0.01$. The loss function is defined in Eq. (5). We use the RGB color space for both low-light and normally-exposed images, and images are converted into the range [-1, 1]. We train on 256×256 random crops with random horizontal flipping. A batch size of 4 is used with an accumulation of gradients for 8 batches in order to simulate a batch size of 32.

The U-Net of the LPDM consists of 4 downsampling stages (encoder) and 4 upsampling stages (decoder), with 2 residual blocks per stage. Between the encoder and the decoder is a middle block which processes the latent encoding. The middle block contains 2 residual blocks which surround a scaled dot-product attention layer using 8 attention heads. We avoid using attention mechanisms at higher resolutions than the final latent encoding in order to conserve memory. Residual blocks within the four downsampling stages output 128, 256, 512 or 512 channels, respectively. Therefore, the residual blocks at the highest resolution output 128 channels, and the latent resolution residual blocks output 512 channels. The residual blocks in the middle block both output 512 channels. The decoder is a reflection of the encoder, where downsampling operations are replaced with upsampling operations and the output of the encoder is concatenated at each upsampling stage.

The implementation of the LPDM method is available online at <https://github.com/savvaki/LPDM>.

C. Benchmark Study for LPDM

The following state-of-the-art LLIE approaches are selected for comparison: LIME [1], BIMEF [14], RetinexNet [25], EnlightenGAN [17], KinD [29], KinD++ [8], ZeroDCE [28], ZeroDCE++ [19], URetinex-Net [18], LLFlow [15] and LLFormer [16]. BIMEF and LIME are non-learning-based methods and the remaining methods are all learning-based. The LLFlow, LLFormer, URetinex-Net and RetinexNet methods are trained on the LOL dataset only. The KinD and KinD++ models are trained on LOL with additional custom synthetic data added [8]. The ZeroDCE and ZeroDCE++ models are trained on multi-exposure image sets from the SICE [59] dataset. EnlightenGAN is trained with unpaired groups of low-light and normal-exposure images using data from LOL as well as additional datasets.

Several methods such as KinD, KinD++, URetinex-Net and LLFlow scale their model outputs based on an illumination ratio which involves the ground truth label. In order to achieve a fair comparison, we do not use the ground truths to scale these model outputs. Instead, we treat the LOL test set as unpaired data as would be the case in real-life scenarios. Similar to previous approaches, we fix the parameters of the LIME algorithm to $\alpha = 0.15$ and $\sigma = 2$ and $\gamma = 0.8$.

We compare the abovementioned LLIE approaches with and without our proposed LPDM. For the remainder of this work, LPDM_s represents the LPDM approach applied with parameter s , defined in Section IV-C. All LPDM results fix $\phi = 300$, and we report two values of s which are 15 and 30. Table I contains results with and without LPDM on the LOL test set represented as $\eta + \text{LPDM}_s$. In addition to the LOL dataset evaluation, we provide qualitative and quantitative results on the abovementioned unpaired test sets. The unpaired test metrics can be found in Table II.

D. Comparison with Alternative Denoisers

We compare the LPDM denoising performance with the popular BM3D [11] algorithm as well as a state-of-the-art DL denoiser NAFNet [12]. Applying BM3D evenly over the entire image results in bright regions being oversmoothed, since noise is often present at higher levels in dark regions. Therefore, previous LLIE works have adapted BM3D to operate unevenly based on the illumination of the recovered image [1], [25].

In particular, we test our method against the denoising approach used in LIME [1]. LIME is a Retinex-based method where the assumption is that $L = R \circ T$, where L represents the source low-light image, R represents the desired recovery image (reflectance), T represents the illumination and \circ represents element-wise multiplication. LIME estimates the illumination T which is then used to determine R given L . In order to avoid oversmoothing bright regions of R , the BM3D algorithm is scaled based on the illumination map T . Furthermore, the BM3D algorithm is only applied to the Y component of R , after R is converted to the YUV color space. The LIME denoising algorithm is as follows [1]:

$$R_f := R \circ T + R_d \circ (1 - T), \quad (9)$$

where R_d is the denoised version of R , and R_f is the recomposed image after weighting R and R_d by T and $1 - T$ respectively. Note that only the Y channel of R in the YUV color space is denoised, and the result is then converted back to the RGB color space to form R_d . We apply LIME to obtain illumination maps T for each low-light image in the LOL test set. We then use Eq. (9), and for each η we set $R = \hat{x}_0^\eta$ for each LOL test example to obtain the denoised result scaled by T . For all figures and tables, BM3D_σ represents the application of the BM3D algorithm according to Eq. (9), where σ is the standard deviation parameter of BM3D. The results are reported in Table I as $\eta + \text{BM3D}_\sigma$.

In a further experiment, we apply a state-of-the-art DL denoiser NAFNet [12] as a post-processing step after LLIE. The NAFNet model is trained on the smartphone image denoising dataset (SIDD) [60] which contains noisy images captured under multiple lighting conditions. Thus, NAFNet is well-suited to denoise enhanced images of a variety of brightness levels. The input to NAFNet is \hat{x}_0^η , and the result is the denoised output which we capture for each η over each test image. The results of NAFNet denoising can be found in Table I represented as $\eta + \text{NAFNet}$.

TABLE I
RESULTS ON THE LOL TEST SET FOR DIFFERENT LLIE METHODS (η), WITH AND WITHOUT POST-PROCESSING.

Methods	SSIM \uparrow	PSNR \uparrow	MAE \downarrow	LPIPS \downarrow	Methods	SSIM \uparrow	PSNR \uparrow	MAE \downarrow	LPIPS \downarrow
LIME [1]	0.484	17.181	0.124	0.372	ZeroDCE [28]	0.562	14.861	0.185	0.335
LIME + BM3D ₅	0.521	17.163	0.126	0.285	ZeroDCE + BM3D ₅	0.593	14.656	0.190	0.220
LIME + BM3D ₁₅	0.543	17.338	0.125	0.218	ZeroDCE + BM3D ₁₅	0.580	14.649	0.190	0.256
LIME + NAFNet	0.753	18.109	0.113	0.249	ZeroDCE + NAFNet	0.689	15.077	0.180	0.287
LIME + LPDM ₁₅	0.687	17.598	0.122	0.195	ZeroDCE + LPDM ₁₅	0.698	14.900	0.187	0.186
LIME + LPDM ₃₀	0.743	17.581	0.122	0.168	ZeroDCE + LPDM ₃₀	0.695	14.839	0.189	0.189
BIMEF [14]	0.595	13.875	0.206	0.326	ZeroDCE++ [19]	0.573	15.357	0.176	0.335
BIMEF + BM3D ₅	0.611	13.653	0.212	0.226	ZeroDCE++ + BM3D ₅	0.605	15.169	0.182	0.214
BIMEF + BM3D ₁₅	0.588	13.619	0.212	0.285	ZeroDCE++ + BM3D ₁₅	0.592	15.167	0.182	0.250
BIMEF + NAFNet	0.662	13.917	0.203	0.309	ZeroDCE++ + NAFNet	0.704	15.628	0.172	0.288
BIMEF + LPDM ₁₅	0.693	13.891	0.210	0.184	ZeroDCE++ + LPDM ₁₅	0.709	15.456	0.179	0.182
BIMEF + LPDM ₃₀	0.685	13.842	0.212	0.192	ZeroDCE++ + LPDM ₃₀	0.708	15.388	0.180	0.183
RetinexNet [22]	0.425	16.774	0.126	0.474	LLFlow [15]	0.852	21.133	0.084	0.119
RetinexNet + BM3D ₅	0.456	16.794	0.126	0.409	LLFlow + BM3D ₅	0.845	21.011	0.085	0.144
RetinexNet + BM3D ₁₅	0.482	17.065	0.123	0.278	LLFlow + BM3D ₁₅	0.830	20.937	0.086	0.189
RetinexNet + NAFNet	0.724	17.636	0.118	0.312	LLFlow + NAFNet	0.808	20.700	0.087	0.214
RetinexNet + LPDM ₁₅	0.649	17.800	0.115	0.264	LLFlow + LPDM ₁₅	0.845	21.165	0.084	0.123
RetinexNet + LPDM ₃₀	0.759	18.017	0.113	0.195	LLFlow + LPDM ₃₀	0.833	21.082	0.084	0.131
EnlightenGAN [17]	0.652	17.483	0.135	0.322	URetinexNet [18]	0.824	19.842	0.099	0.128
EnlightenGAN + BM3D ₅	0.715	17.332	0.139	0.220	URetinexNet + BM3D ₅	0.824	19.784	0.099	0.156
EnlightenGAN + BM3D ₁₅	0.721	17.358	0.139	0.247	URetinexNet + BM3D ₁₅	0.806	19.727	0.099	0.206
EnlightenGAN + NAFNet	0.741	17.618	0.133	0.242	URetinexNet + NAFNet	0.791	19.487	0.101	0.216
EnlightenGAN + LPDM ₁₅	0.761	17.560	0.136	0.170	URetinexNet + LPDM ₁₅	0.829	20.067	0.097	0.135
EnlightenGAN + LPDM ₃₀	0.757	17.483	0.137	0.180	URetinexNet + LPDM ₃₀	0.822	20.120	0.096	0.142
KinD [29]	0.771	17.648	0.123	0.175	LLFormer [16]	0.819	23.346	0.067	0.168
KinD + BM3D ₅	0.771	17.497	0.125	0.193	LLFormer + BM3D ₅	0.832	23.110	0.068	0.178
KinD + BM3D ₁₅	0.761	17.482	0.126	0.233	LLFormer + BM3D ₁₅	0.816	22.962	0.069	0.228
KinD + NAFNet	0.761	17.570	0.124	0.252	LLFormer + NAFNet	0.807	22.799	0.069	0.234
KinD + LPDM ₁₅	0.794	17.656	0.124	0.153	LLFormer + LPDM ₁₅	0.859	23.750	0.066	0.113
KinD + LPDM ₃₀	0.787	17.603	0.125	0.158	LLFormer + LPDM ₃₀	0.854	23.629	0.066	0.120
KinD++ [8]	0.758	17.752	0.113	0.198					
KinD++ + BM3D ₅	0.768	17.714	0.113	0.203					
KinD++ + BM3D ₁₅	0.769	17.740	0.113	0.224					
KinD++ + NAFNet	0.765	17.768	0.114	0.245					
KinD++ + LPDM ₁₅	0.796	17.823	0.112	0.170					
KinD++ + LPDM ₃₀	0.795	17.786	0.112	0.175					

E. Interpretation of Results

The full-reference and no-reference metrics are reported in Table I and Table II, respectively. Metrics marked in bold indicate that they are the best for a particular method. The LOL test set results in Table I show that our LPDM is able to improve the SSIM of all baseline LLIE methods except LLFlow on the LOL dataset. In all cases, LPDM improves the PSNR compared to each baseline. In many cases, the SSIM is greatly improved by adding the LPDM. Adding the LPDM to LIME, RetinexNet, EnlightenGAN, ZeroDCE, ZeroDCE++ and LLFormer boasts up to a 53.5%, 78.65%, 16.8%, 24.08%, 23.82%, 4.92% SSIM improvement, respectively. LLFormer yields new state-of-the-art color SSIM results on the LOL dataset when LPDM post-processing is added.

LPDM is able to improve the baseline PSNR for all methods, and mostly outperforms the competing denoisers on the PSNR metric. In all cases, LPDM outperforms the alternative denoisers on the perceptual LPIPS metric. In some cases, NAFNet is able to improve PSNR and MAE more than our LPDM; however, upon further inspection, this is

as a result of aggressive denoising and thus oversmoothing. Fig. 5 displays a comparison of post-processing approaches. NAFNet removes most typical noises, however at the cost of removing detail. For example, consider the first row of Fig. 5, where technically NAFNet yields a higher PSNR for \hat{x}_0^{LIME} , but the results are clearly blurred when compared to LPDM which maintains the sharpness of the original image. The behavior of NAFNet manifests more accurately in the LPIPS metric where the LPDM outperforms NAFNet significantly for all LLIE methods. In addition, the BM3D denoiser performs well, however it is unable to deal with color noises and other distortions as robustly as DL methods.

Notably, NAFNet only performs better than LPDM for SSIM on the noise introduced by the LIME method due to the type of noise being similar to most denoising datasets. In contrast, our method models the conditional distribution between low-light and normally-exposed images, and thus the LPDM can handle a variety of different artifacts and color distortions besides typical noise. An example of a distortion which differs from typical Gaussian noise is the distortion

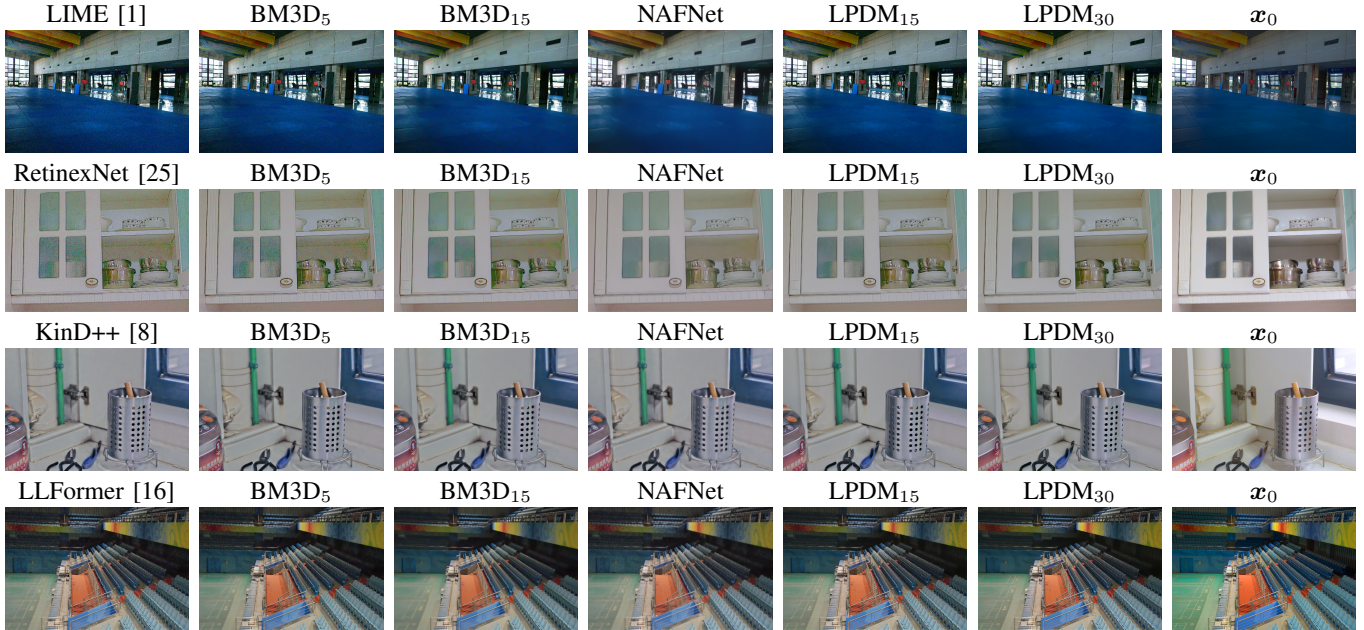


Fig. 5. A qualitative comparison of the BM3D [11] and NAFNet [12] post-processing denoising approaches to LPDM on the LOL test set. The first column displays \hat{x}_0^η for different η . The final column contains the ground truth label. The remaining columns display the results of different denoising approaches which post-process \hat{x}_0^η .

introduced by KinD++. Row three of Fig. 5 displays how our LPDM increases the sharpness of $\hat{x}_0^{\text{KinD++}}$ where the other denoisers yield oversmoothed results. We emphasize this point because different LLIE methods introduce a panoply of different distortions.

For the majority of methods and datasets in Table II, LPDM is able to improve the SPAQ score. The improvement of the NIQE score and BRISQUE score fluctuates depending on the dataset and the method. Therefore, it is vital to analyze the qualitative effects of LPDM on real test data. Several images from a variety of datasets are displayed in Fig. 1. The general advantage of LPDM is its ability to strike a balance between smoothing and maintaining sharpness. Due to the distribution of the noise output of LPDM being zero-centered, our approach maintains the perceptual quality of the underlying image and avoids oversmoothing when Eq. (8) is applied. In some cases, the LPDM is able to improve color quality and sharpness. Upon close inspection, LPDM alters color shades to more accurately represent reality, as seen for BIMEF, KinD++, LLFormer and URetinex-Net examples in Fig. 1.

In addition to the above conclusions, the choices of $s = 15$ and $s = 30$ may not necessarily be the optimal values for each LLIE method. Therefore, there may be larger improvements for a different choice of s which can be determined empirically. We fix s in order to demonstrate the possibility of using the LPDM as a blind denoiser.

F. Ablation Study

An ablation study is necessary in order to demonstrate that the improvements of LPDM can be attributed specifically to our proposed approach and that the results are not arbitrary. In Section V-F1 we examine the effect of predicting ϵ , and in

Section V-F2 we compare unconditional diffusion to LPDM. In order to conserve space, tables for the ablation study results are summarized such that the percentage improvement for each metric is calculated for each η , and the mean and standard deviation percentage improvements are reported.

1) *The Effect of Predicting the Noise:* As seen in Eq. (5), DMs are trained to make predictions for ϵ . We examine the value of predicting ϵ by changing the model to predict x_0 directly, and we name this model *direct* LPDM or DLPDM. The DLPDM model directly denoises the input and does not require any further steps such as Eq. (8). The DLPDM is identical to the LPDM described in Section V-B with two differences: the ground truth target of the model is now x_0 rather than ϵ , and we remove timestep conditioning from the model by setting $t = 0$ as input to the model regardless of x_t . Therefore, the model directly denoises its input with the same number of parameters and without the requirement of specifying ϕ at inference time, thus making the model a blind denoiser. In other terms, the model is responsible for detecting the amount of noise present in x_t and predicting x_0 without any additional parameters defined by the user.

The results of the DLPDM experiment are summarized in Table III, which includes the other ablation results from Section V-F2. Our proposed LPDM approach performs better on SSIM and LPIPS and DLPDM performs better on PSNR and MAE (although the variance of DLPDM is higher). LPDM largely outperforms DLPDM on LPIPS which implies that LPDM results are more perceptually similar to the ground truth. The results are verified when examining the examples in Fig. 6 where LPDM preserves the sharpness of \hat{x}_0^η and maintains color accuracy.

2) *The Effect of Conditioning:* We explore the effect of appending c to x_t as visually depicted in Fig. 4. We name

TABLE II
RESULTS ON UNPAIRED TEST SETS FOR DIFFERENT LLIE METHODS (η), WITH AND WITHOUT OUR PROPOSED LPDM.

Method	LIME [1]			DICM [52]			MEF [53]			NPE [54]		
	NIQE ↓	BRISQUE ↓	SPAQ ↑	NIQE ↓	BRISQUE ↓	SPAQ ↑	NIQE ↓	BRISQUE ↓	SPAQ ↑	NIQE ↓	BRISQUE ↓	SPAQ ↑
LIME	4.083	18.977	64.485	3.812	23.356	63.301	3.558	16.337	70.911	4.196	17.296	73.505
LIME + LPDM ₁₅	4.194	17.383	68.573	3.783	23.436	66.104	3.677	18.434	71.938	4.152	16.522	73.775
LIME + LPDM ₃₀	4.354	21.625	70.491	4.013	23.810	66.957	4.248	24.732	71.848	4.465	20.773	73.796
BIMEF	3.859	17.714	65.121	3.827	23.588	64.375	3.330	15.262	67.352	4.135	14.928	72.622
BIMEF + LPDM ₁₅	4.140	18.182	68.242	3.872	21.827	68.191	3.756	20.484	68.502	4.123	16.363	74.092
BIMEF + LPDM ₃₀	4.261	21.886	68.768	4.059	23.522	69.013	4.394	24.851	68.288	4.345	19.518	74.631
RetinexNet	4.598	26.341	70.370	4.451	29.339	68.805	4.416	20.068	74.386	4.595	22.579	74.910
RetinexNet + LPDM ₁₅	4.527	22.475	70.117	4.219	23.877	69.707	3.785	14.983	73.337	4.400	19.791	74.347
RetinexNet + LPDM ₃₀	4.642	24.404	70.220	4.173	24.105	69.953	4.287	24.093	72.105	4.690	23.528	74.524
EnlightenGAN	3.657	14.879	64.208	3.561	18.808	63.124	3.221	14.332	68.701	4.116	15.344	73.552
EnlightenGAN + LPDM ₁₅	4.093	17.026	68.037	3.828	20.201	66.434	3.695	19.659	70.896	4.096	17.130	74.421
EnlightenGAN + LPDM ₃₀	4.196	20.784	69.222	4.012	23.602	67.265	4.293	24.603	71.092	4.316	18.633	74.407
KinD	4.762	25.208	64.511	4.139	29.116	65.324	3.875	27.500	66.879	4.167	18.092	74.067
KinD + LPDM ₁₅	4.080	21.051	67.512	4.057	26.786	67.934	4.097	26.366	68.920	4.205	17.912	73.596
KinD + LPDM ₃₀	4.140	20.834	68.483	4.039	26.447	68.380	4.259	26.296	69.117	4.317	19.885	73.392
KinD++	4.726	23.298	65.992	3.786	26.314	68.086	3.737	28.635	70.250	4.384	20.970	75.817
KinD++ + LPDM ₁₅	4.162	22.430	68.063	3.928	26.557	68.615	3.996	28.199	69.719	4.237	19.551	74.419
KinD++ + LPDM ₃₀	4.277	22.636	69.059	3.987	27.188	68.549	4.321	28.823	69.179	4.403	22.253	73.892
ZeroDCE	3.773	18.480	64.883	3.723	23.519	64.769	3.283	16.632	70.906	3.946	15.739	74.399
ZeroDCE + LPDM ₁₅	4.133	18.665	68.409	3.800	20.434	68.014	3.625	19.312	70.895	3.991	16.709	74.049
ZeroDCE + LPDM ₃₀	4.274	22.588	69.197	4.029	24.862	68.533	4.371	25.448	70.202	4.285	19.599	73.981
ZeroDCE++	3.965	17.217	64.956	3.824	21.368	64.470	3.400	13.602	70.291	4.021	12.941	73.658
ZeroDCE++ + LPDM ₁₅	4.212	18.119	68.771	3.836	19.833	68.150	3.680	18.977	70.718	4.065	15.900	74.319
ZeroDCE++ + LPDM ₃₀	4.344	21.864	69.743	4.012	24.171	68.938	4.336	24.742	70.305	4.308	18.937	74.245
LLFlow	5.071	26.596	68.282	3.831	24.895	67.698	3.924	26.973	72.368	4.203	19.680	73.812
LLFlow + LPDM ₁₅	4.439	22.743	69.879	3.883	22.716	69.366	3.987	25.713	70.431	4.231	18.306	73.752
LLFlow + LPDM ₃₀	4.288	21.087	70.587	3.877	21.569	69.742	4.153	24.973	69.944	4.278	17.640	73.812
URetinexNet	4.353	23.906	68.232	4.152	24.261	66.239	3.790	21.478	72.005	4.688	24.384	74.462
URetinexNet + LPDM ₁₅	4.321	23.230	69.090	3.947	24.836	66.936	3.954	24.841	71.162	4.429	22.919	74.295
URetinexNet + LPDM ₃₀	4.275	22.151	68.814	3.984	25.737	66.870	4.098	24.628	70.503	4.392	23.557	73.880
LLFormer	4.145	14.664	61.821	3.850	14.610	63.080	3.682	17.043	63.139	3.962	12.440	71.975
LLFormer + LPDM ₁₅	4.036	18.341	66.215	3.876	20.341	68.142	3.890	21.707	69.204	4.097	15.085	74.386
LLFormer + LPDM ₃₀	4.064	18.529	67.494	3.815	18.538	69.126	3.970	20.358	70.377	4.128	13.371	74.728

TABLE III
ABLATION STUDY COMPARING LPDM TO DLPDM AND ULPDM ON THE LOL TEST SET.

Methods	SSIM (%) ↑	PSNR (%) ↑	MAE (%) ↑	LPIPS (%) ↑
DLPDM	19.218 ± 26.84	2.53 ± 3.4	2.531 ± 4.93	18.798 ± 23.76
ULPDM ₁₅	1.937 ± 28.55	-0.317 ± 2.42	-0.687 ± 3.33	-8.43 ± 39.76
ULPDM ₃₀	-17.566 ± 28.42	-2.096 ± 3.27	-2.754 ± 4.95	-43.713 ± 53.83
LPDM ₁₅	17.138 ± 17.50	1.225 ± 1.79	0.942 ± 2.92	29.462 ± 20.96
LPDM ₃₀	19.928 ± 25.17	1.079 ± 2.26	0.657 ± 3.66	28.820 ± 24.94

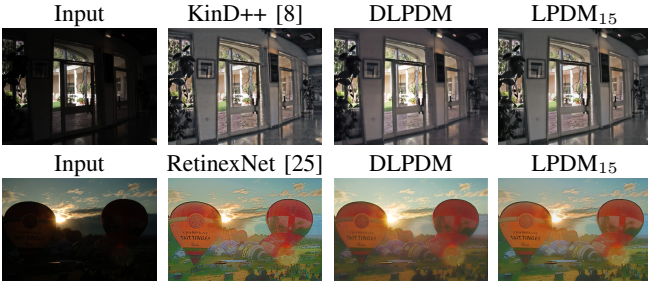


Fig. 6. Visual examples of the ablation study directly comparing predicting \hat{x}_0 to predicting ϵ using the DLPDM and LPDM models, respectively.

this model *unconditional* LPDM or ULPDM. In many cases, diffusion models may ignore the concatenated conditioning and simply learn how to denoise. Therefore, it is important to explore whether the LPDM requires the use of conditioning to achieve the desired results. ULPDM is an identical model to LPDM from Section V-B, however, we change the input

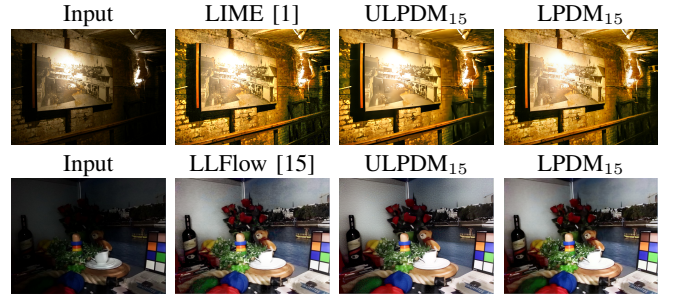


Fig. 7. Visual examples of the ablation study comparing unconditional and conditional diffusion using the ULPDM and LPDM models, respectively.

layer to accept only x_t as input, thus changing the number of input channels from six to three. In other terms, we compare conditional diffusion to unconditional diffusion.

The experimental results in Table III show that LPDM significantly outperforms ULPDM across all metrics. Therefore, we conclude that conditioning is necessary in order for the LPDM to detect the wide variety of artifacts that can be present in \hat{x}_0^η . We provide visual results in Fig. 7 which verify our conclusion: ULPDM is able to remove noise, however results are oversmoothed and thus detail is lost due to lack of conditioning.

VI. CONCLUSION

In this paper, we present a framework for post-processing images which have undergone low-light image enhancement.

The enhancement of low-light images often reveals a variety of degradations which are hidden in the dark, and thus a need for post-processing is introduced. Furthermore, each low-light enhancement technique can possibly introduce a different form of degradation into its result. We propose using a conditional diffusion model in order to model the distribution between under-exposed and normally-exposed images. Further, we introduce a method of applying the diffusion model as a post-processing technique. Our approach uses the diffusion model to estimate the amount of noise present in an enhanced image in one pass through the model, which can simply be subtracted from the enhanced image to further enhance the image. Moreover, we demonstrate that our approach outperforms competing post-processing denoisers, and we demonstrate its versatility on a variety of low-light datasets with different state-of-the-art low-light image enhancement backbones. In contrast to existing denoisers, we find that our approach is able to improve perceptual quality, while removing noise and other distortions. In future work, our approach could potentially be applied to other image restoration domains.

ACKNOWLEDGMENT

This study was supported by the National Research Foundation (NRF), South Africa, Thuthuka Grant Number 13819413. The authors acknowledge the Centre for High Performance Computing (CHPC), South Africa, for providing computational resources to this research project.

REFERENCES

- [1] X. Guo, Y. Li, and H. Ling, "Lime: Low-light image enhancement via illumination map estimation," *IEEE Transactions on Image Processing*, vol. 26, no. 2, pp. 982–993, 2017.
- [2] Y. Sasagawa and H. Nagahara, "Yolo in the dark-domain adaptation method for merging multiple models," in *Computer Vision—ECCV 2020: 16th European Conference, Glasgow, UK, August 23–28, 2020, Proceedings, Part XXI 16*. Springer, 2020, pp. 345–359.
- [3] J. Liu, D. Xu, W. Yang, M. Fan, and H. Huang, "Benchmarking low-light image enhancement and beyond," *International Journal of Computer Vision*, vol. 129, pp. 1153–1184, 2021.
- [4] K. G. Lore, A. Akintayo, and S. Sarkar, "Llnet: A deep autoencoder approach to natural low-light image enhancement," *Pattern Recognition*, vol. 61, pp. 650–662, 2017.
- [5] S. Zheng and G. Gupta, "Semantic-guided zero-shot learning for low-light image/video enhancement," in *Proceedings of the IEEE/CVF Winter Conference on Applications of Computer Vision*, 2022, pp. 581–590.
- [6] S. M. Pizer, E. P. Amburn, J. D. Austin, R. Cromartie, A. Geselowitz, T. Greer, B. ter Haar Romeny, J. B. Zimmerman, and K. Zuiderveld, "Adaptive histogram equalization and its variations," *Computer vision, graphics, and image processing*, vol. 39, no. 3, pp. 355–368, 1987.
- [7] C. Chen, Q. Chen, J. Xu, and V. Koltun, "Learning to see in the dark," in *Proceedings of the IEEE Conference on Computer Vision and Pattern Recognition*, 2018, pp. 3291–3300.
- [8] Y. Zhang, X. Guo, J. Ma, W. Liu, and J. Zhang, "Beyond brightening low-light images," *International Journal of Computer Vision*, vol. 129, pp. 1013–1037, 2021.
- [9] Y. Zhou, J. Jiao, H. Huang, Y. Wang, J. Wang, H. Shi, and T. Huang, "When awgn-based denoiser meets real noises," in *Proceedings of the AAAI Conference on Artificial Intelligence*, vol. 34, no. 07, 2020, pp. 13 074–13 081.
- [10] L. Li, R. Wang, W. Wang, and W. Gao, "A low-light image enhancement method for both denoising and contrast enlarging," in *2015 IEEE international conference on image processing (ICIP)*. IEEE, 2015, pp. 3730–3734.
- [11] K. Dabov, A. Foi, V. Katkovnik, and K. Egiazarian, "Image denoising by sparse 3-d transform-domain collaborative filtering," *IEEE Transactions on Image Processing*, vol. 16, no. 8, pp. 2080–2095, 2007.
- [12] L. Chen, X. Chu, X. Zhang, and J. Sun, "Simple baselines for image restoration," in *Computer Vision—ECCV 2022: 17th European Conference, Tel Aviv, Israel, October 23–27, 2022, Proceedings, Part VII*. Springer, 2022, pp. 17–33.
- [13] J. Ho, A. Jain, and P. Abbeel, "Denoising diffusion probabilistic models," in *Advances in Neural Information Processing Systems*, H. Larochelle, M. Ranzato, R. Hadsell, M. Balcan, and H. Lin, Eds., vol. 33. Curran Associates, Inc., 2020, pp. 6840–6851. [Online]. Available: <https://proceedings.neurips.cc/paper/2020/file/4c5bcfec8584af0d967f1ab10179ca4b-Paper.pdf>
- [14] Z. Ying, G. Li, and W. Gao, "A bio-inspired multi-exposure fusion framework for low-light image enhancement," *arXiv preprint arXiv:1711.00591*, 2017.
- [15] Y. Wang, R. Wan, W. Yang, H. Li, L.-P. Chau, and A. Kot, "Low-light image enhancement with normalizing flow," in *Proceedings of the AAAI Conference on Artificial Intelligence*, vol. 36, no. 3, 2022, pp. 2604–2612.
- [16] T. Wang, K. Zhang, T. Shen, W. Luo, B. Stenger, and T. Lu, "Ultra-high-definition low-light image enhancement: A benchmark and transformer-based method," *arXiv preprint arXiv:2212.11548*, 2022.
- [17] Y. Jiang, X. Gong, D. Liu, Y. Cheng, C. Fang, X. Shen, J. Yang, P. Zhou, and Z. Wang, "Enlightengan: Deep light enhancement without paired supervision," *IEEE Transactions on Image Processing*, vol. 30, pp. 2340–2349, 2021.
- [18] W. Wu, J. Weng, P. Zhang, X. Wang, W. Yang, and J. Jiang, "Uretinex-net: Retinex-based deep unfolding network for low-light image enhancement," in *2022 IEEE/CVF Conference on Computer Vision and Pattern Recognition (CVPR)*, 2022, pp. 5891–5900.
- [19] C. Li, C. Guo, and C. C. Loy, "Learning to enhance low-light image via zero-reference deep curve estimation," *IEEE Transactions on Pattern Analysis and Machine Intelligence*, vol. 44, no. 8, pp. 4225–4238, 2021.
- [20] J. A. Stark, "Adaptive image contrast enhancement using generalizations of histogram equalization," *IEEE Transactions on Image Processing*, vol. 9, no. 5, pp. 889–896, 2000.
- [21] S. Rahman, M. M. Rahman, M. Abdullah-Al-Wadud, G. D. Al-Quaderi, and M. Shoyaib, "An adaptive gamma correction for image enhancement," *EURASIP Journal on Image and Video Processing*, vol. 2016, no. 1, pp. 1–13, 2016.
- [22] E. H. Land and J. J. McCann, "Lightness and retinex theory," *Josa*, vol. 61, no. 1, pp. 1–11, 1971.
- [23] M. Li, J. Liu, W. Yang, X. Sun, and Z. Guo, "Structure-revealing low-light image enhancement via robust retinex model," *IEEE Transactions on Image Processing*, vol. 27, no. 6, pp. 2828–2841, 2018.
- [24] A. Vaswani, N. Shazeer, N. Parmar, J. Uszkoreit, L. Jones, A. N. Gomez, Ł. Kaiser, and I. Polosukhin, "Attention is all you need," *Advances in neural information processing systems*, vol. 30, 2017.
- [25] C. Wei, W. Wang, W. Yang, and J. Liu, "Deep retinex decomposition for low-light enhancement," in *British Machine Vision Conference*, 2018.
- [26] J. Cai, S. Gu, and L. Zhang, "Learning a deep single image contrast enhancer from multi-exposure images," *IEEE Transactions on Image Processing*, vol. 27, no. 4, pp. 2049–2062, 2018.
- [27] R. Wang, Q. Zhang, C.-W. Fu, X. Shen, W.-S. Zheng, and J. Jia, "Underexposed photo enhancement using deep illumination estimation," in *Proceedings of the IEEE/CVF conference on computer vision and pattern recognition*, 2019, pp. 6849–6857.
- [28] C. Guo, C. Li, J. Guo, C. C. Loy, J. Hou, S. Kwong, and R. Cong, "Zero-reference deep curve estimation for low-light image enhancement," in *Proceedings of the IEEE/CVF Conference on Computer Vision and Pattern Recognition (CVPR)*, June 2020.
- [29] Y. Zhang, J. Zhang, and X. Guo, "Kindling the darkness: A practical low-light image enhancer," in *Proceedings of the 27th ACM international conference on multimedia*, 2019, pp. 1632–1640.
- [30] W. Yang, S. Wang, Y. Fang, Y. Wang, and J. Liu, "From fidelity to perceptual quality: A semi-supervised approach for low-light image enhancement," in *IEEE/CVF Conference on Computer Vision and Pattern Recognition (CVPR)*, June 2020.
- [31] J. Johnson, A. Alahi, and L. Fei-Fei, "Perceptual losses for real-time style transfer and super-resolution," in *Computer Vision—ECCV 2016: 14th European Conference, Amsterdam, The Netherlands, October 11–14, 2016, Proceedings, Part II 14*. Springer, 2016, pp. 694–711.
- [32] X. Wei, X. Zhang, and Y. Li, "Sarn: A lightweight stacked attention residual network for low-light image enhancement," in *2021 6th International Conference on Robotics and Automation Engineering (ICRAE)*, 2021, pp. 275–279.
- [33] S. W. Zamir, A. Arora, S. Khan, M. Hayat, F. S. Khan, and M.-H. Yang, "Restormer: Efficient transformer for high-resolution image restoration," in *CVPR*, 2022.

- [34] I. Kobyzev, S. J. Prince, and M. A. Brubaker, "Normalizing flows: An introduction and review of current methods," *IEEE Transactions on Pattern Analysis and Machine Intelligence*, vol. 43, no. 11, pp. 3964–3979, 2020.
- [35] J. Sohl-Dickstein, E. Weiss, N. Maheswaranathan, and S. Ganguli, "Deep unsupervised learning using nonequilibrium thermodynamics," in *International Conference on Machine Learning*. PMLR, 2015, pp. 2256–2265.
- [36] A. Q. Nichol and P. Dhariwal, "Improved denoising diffusion probabilistic models," in *Proceedings of the 38th International Conference on Machine Learning*, ser. Proceedings of Machine Learning Research, M. Meila and T. Zhang, Eds., vol. 139. PMLR, 18–24 Jul 2021, pp. 8162–8171. [Online]. Available: <https://proceedings.mlr.press/v139/nichol21a.html>
- [37] P. Dhariwal and A. Nichol, "Diffusion models beat gans on image synthesis," in *Advances in Neural Information Processing Systems*, M. Ranzato, A. Beygelzimer, Y. Dauphin, P. Liang, and J. W. Vaughan, Eds., vol. 34. Curran Associates, Inc., 2021, pp. 8780–8794. [Online]. Available: <https://proceedings.neurips.cc/paper/2021/file/49ad23d1ec9fa4bd8d77d02681df5cfa-Paper.pdf>
- [38] J. Ho and T. Salimans, "Classifier-free diffusion guidance," in *NeurIPS 2021 Workshop on Deep Generative Models and Downstream Applications*, 2021. [Online]. Available: <https://openreview.net/forum?id=qw8AKxfYbI>
- [39] J. Song, C. Meng, and S. Ermon, "Denoising diffusion implicit models," in *International Conference on Learning Representations*, 2021. [Online]. Available: <https://openreview.net/forum?id=StlgiaRCHLP>
- [40] R. Rombach, A. Blattmann, D. Lorenz, P. Esser, and B. Ommer, "High-resolution image synthesis with latent diffusion models," in *Proceedings of the IEEE/CVF Conference on Computer Vision and Pattern Recognition*, 2022, pp. 10 684–10 695.
- [41] B. Kim, Y. Oh, and J. C. Ye, "Diffusion adversarial representation learning for self-supervised vessel segmentation," in *International Conference on Learning Representations*, 2023. [Online]. Available: <https://openreview.net/forum?id=H0gdPxSwkPb>
- [42] B. Kim, I. Han, and J. C. Ye, "Diffusemorph: Unsupervised deformable image registration using diffusion model," in *Computer Vision – ECCV 2022*, S. Avidan, G. Brostow, M. Cissé, G. M. Farinella, and T. Hassner, Eds. Cham: Springer Nature Switzerland, 2022, pp. 347–364.
- [43] E. A. Brempont, S. Kornblith, T. Chen, N. Parmar, M. Minderer, and M. Norouzi, "Denoising pretraining for semantic segmentation," in *Proceedings of the IEEE/CVF Conference on Computer Vision and Pattern Recognition*, 2022, pp. 4175–4186.
- [44] O. Ronneberger, P. Fischer, and T. Brox, "U-net: Convolutional networks for biomedical image segmentation," in *Medical Image Computing and Computer-Assisted Intervention–MICCAI 2015: 18th International Conference, Munich, Germany, October 5–9, 2015, Proceedings, Part III 18*. Springer, 2015, pp. 234–241.
- [45] K. He, X. Zhang, S. Ren, and J. Sun, "Deep residual learning for image recognition," in *Proceedings of the IEEE Conference on Computer Vision and Pattern Recognition*, 2016, pp. 770–778.
- [46] Y. Wu and K. He, "Group normalization," in *Proceedings of the European conference on computer vision (ECCV)*, 2018, pp. 3–19.
- [47] S. Elfving, E. Uchibe, and K. Doya, "Sigmoid-weighted linear units for neural network function approximation in reinforcement learning," *Neural Networks*, vol. 107, pp. 3–11, 2018.
- [48] I. Beltagy, M. E. Peters, and A. Cohan, "Longformer: The long-document transformer," *arXiv:2004.05150*, 2020.
- [49] C.-F. R. Chen, Q. Fan, and R. Panda, "Crossvit: Cross-attention multi-scale vision transformer for image classification," in *Proceedings of the IEEE/CVF international conference on computer vision*, 2021, pp. 357–366.
- [50] W. Yang, W. Wang, H. Huang, S. Wang, and J. Liu, "Sparse gradient regularized deep retinex network for robust low-light image enhancement," *IEEE Transactions on Image Processing*, vol. 30, pp. 2072–2086, 2021.
- [51] C. Lee, C. Lee, and C.-S. Kim, "Contrast enhancement based on layered difference representation of 2d histograms," *IEEE Transactions on Image Processing*, vol. 22, no. 12, pp. 5372–5384, 2013.
- [52] K. Ma, K. Zeng, and Z. Wang, "Perceptual quality assessment for multi-exposure image fusion," *IEEE Transactions on Image Processing*, vol. 24, no. 11, pp. 3345–3356, 2015.
- [53] S. Wang, J. Zheng, H.-M. Hu, and B. Li, "Naturalness preserved enhancement algorithm for non-uniform illumination images," *IEEE Transactions on Image Processing*, vol. 22, no. 9, pp. 3538–3548, 2013.
- [54] R. Zhang, P. Isola, A. A. Efros, E. Shechtman, and O. Wang, "The unreasonable effectiveness of deep features as a perceptual metric," in *Proceedings of the IEEE Conference on Computer Vision and Pattern Recognition*, 2018, pp. 586–595.
- [55] A. Mittal, R. Soundararajan, and A. C. Bovik, "Making a "completely blind" image quality analyzer," *IEEE Signal Processing Letters*, vol. 20, no. 3, pp. 209–212, 2013.
- [56] A. Mittal, A. K. Moorthy, and A. C. Bovik, "No-reference image quality assessment in the spatial domain," *IEEE Transactions on Image Processing*, vol. 21, no. 12, pp. 4695–4708, 2012.
- [57] Y. Fang, H. Zhu, Y. Zeng, K. Ma, and Z. Wang, "Perceptual quality assessment of smartphone photography," in *Proceedings of the IEEE/CVF Conference on Computer Vision and Pattern Recognition*, 2020, pp. 3677–3686.
- [58] I. Loshchilov and F. Hutter, "Decoupled weight decay regularization," in *International Conference on Learning Representations*, 2019. [Online]. Available: <https://openreview.net/forum?id=Bkg6RiCqY7>
- [59] J. Cai, S. Gu, and L. Zhang, "Learning a deep single image contrast enhancer from multi-exposure images," *IEEE Transactions on Image Processing*, vol. 27, no. 4, pp. 2049–2062, 2018.
- [60] A. Abdelhamed, S. Lin, and M. S. Brown, "A high-quality denoising dataset for smartphone cameras," in *Proceedings of the IEEE Conference on Computer Vision and Pattern Recognition*, 2018, pp. 1692–1700.